

Benzylammonium-Mediated Formamidinium Lead Iodide Perovskite Phase Stabilization for Photovoltaics

Anwar Q. Alanazi, Masaud H. Almalki, Aditya Mishra, Dominik J. Kubicki, Zaiwei Wang, Lena Merten, Felix T. Eickemeyer, Hong Zhang, Dan Ren, Ahmed Y. Alyamani, Hamad Albrithen, Abdulrahman Albadri, Mohammad Hayal Alotaibi, Alexander Hinderhofer, Shaik M. Zakeeruddin, Frank Schreiber, Anders Hagfeldt, Lyndon Emsley,* Jovana V. Milić,* and Michael Graetzel*

There is an ongoing surge of interest in the use of formamidinium (FA) lead iodide perovskites in photovoltaics due to their exceptional optoelectronic properties. However, thermodynamic instability of the desired cubic perovskite (α -FAPbI₃) phase at ambient conditions leads to the formation of a yellow non-perovskite (δ -FAPbI₃) phase that compromises its utility. A stable α -FAPbI₃ perovskite phase is achieved by employing benzylammonium iodide (BzI) and the microscopic structure is elucidated by using solid-state NMR spectroscopy and X-ray scattering measurements. Perovskite solar cells based on the FAPbI₃(BzI)_{0.25} composition achieve power conversion efficiencies exceeding 20%, which is accompanied by enhanced shelf-life and operational stability, maintaining 80% of the performance after one year at ambient conditions.

over the last decade, rising from 3.8% to over 25%.^[1,2] This stunning improvement can be ascribed to the perovskite absorber materials, which are ionic crystals possessing high dielectric constants, long charge carrier diffusion lengths, large absorption coefficients, and a bandgap suitable for solar light harvesting.^[3–8] These materials are based on the ABX₃ structure (Figure 1a,b), where A is a monovalent cation, e.g., organic methylammonium (MA), formamidinium (FA), or inorganic Cs⁺, B is a divalent metal (such as Pb²⁺ or Sn²⁺), and X is a halide ion (Cl⁻, Br⁻, or I⁻).^[9] Perovskite properties are tunable by replacing the large halide (e.g., I⁻) by smaller size halides (e.g., Br⁻),

which results in an increase in the bandgap,^[10] while substituting Pb²⁺ by Sn²⁺ decreases the bandgap.^[11]

Another approach to tailoring the optoelectronic properties includes the use of larger organic cations to form


1. Introduction

Hybrid organic–inorganic perovskite solar cells (PSCs) have seen an unprecedented increase in photovoltaic performance

A. Q. Alanazi, M. H. Almalki, Dr. D. J. Kubicki, Dr. F. T. Eickemeyer, Dr. H. Zhang, Dr. D. Ren, Dr. S. M. Zakeeruddin, Dr. J. V. Milić, Prof. M. Graetzel
Laboratory of Photonics and Interfaces
Institute of Chemical Sciences and Engineering
School of Basic Sciences
Ecole Polytechnique Fédérale de Lausanne
Lausanne CH-1015, Switzerland
E-mail: jovana.milic@epfl.ch; michael.graetzel@epfl.ch

A. Mishra, Dr. D. J. Kubicki, Prof. L. Emsley
Laboratory of Magnetic Resonance
Institute of Chemical Sciences and Engineering
School of Basic Sciences
Ecole Polytechnique Fédérale de Lausanne
Lausanne CH-1015, Switzerland
E-mail: lyndon.emsley@epfl.ch

Dr. Z. Wang, Prof. A. Hagfeldt
Laboratory of Photomolecular Science
Institute of Chemical Sciences Engineering
Ecole Polytechnique Fédérale de Lausanne (EPFL)
Lausanne 1015, Switzerland

 The ORCID identification number(s) for the author(s) of this article can be found under <https://doi.org/10.1002/adfm.202101163>.

L. Merten, Dr. A. Hinderhofer, Prof. F. Schreiber
Institut für Angewandte Physik
Universität Tübingen
Auf der Morgenstelle 10, 72076 Tübingen, Germany

Dr. A. Y. Alyamani, Dr. H. Albrithen, Dr. A. Albadri, Dr. M. H. Alotaibi
National Center for Nanotechnology
King Abdulaziz City for Science and Technology
P.O. Box 6086, Riyadh 11442, Saudi Arabia

Dr. H. Albrithen
Physics and Astronomy Department-Research Chair for Tribology
Surface and Interface Sciences
College of Science and King Abdullah Institute for
Nanotechnology-Aramco Laboratory for Applied Sensing Research
King Saud University
P.O. Box 2455, Riyadh 11451, Saudi Arabia

Dr. H. Albrithen
K.A.CARE Energy Research and Innovation Center at Riyadh
Riyadh 11451, Saudi Arabia

DOI: 10.1002/adfm.202101163

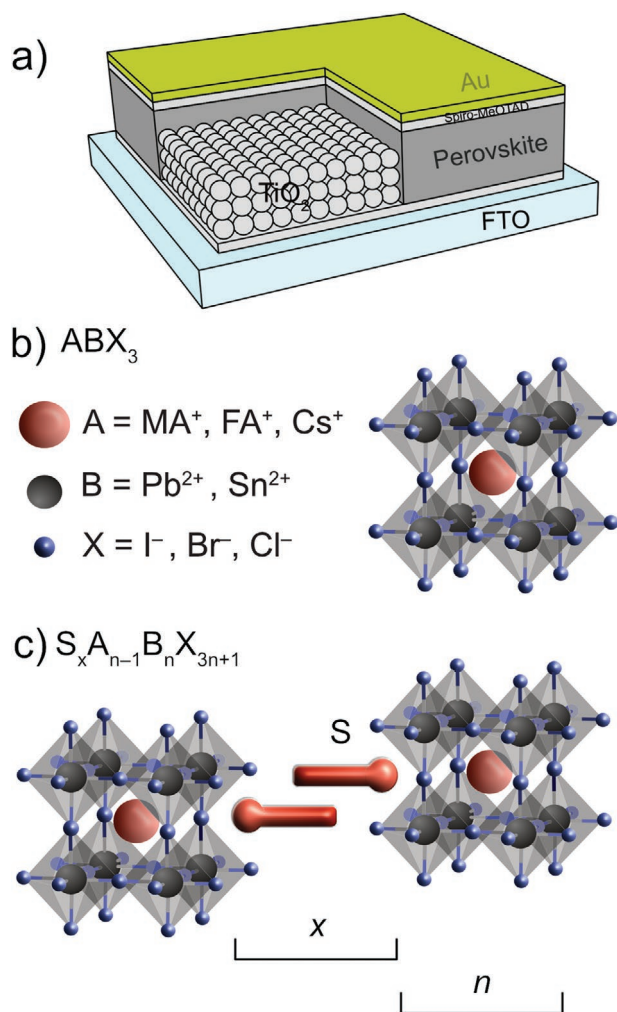


Figure 1. Schematic representation of a) a perovskite solar cell as well as b) the 3D perovskite crystal structure based on an ABX₃ formulation along with c) the typical layered 2D perovskite structure based on S_xA_{n-1}B_nX_{3n+1} formula. For instance, the presented 2D structure can be defined by the $x = 2$ and $n = 2$ composition forming a Ruddlesden-Popper phase.

low-dimensional perovskites.^[12,13] This approach leads to an increase in the bandgap as a result of modifying the 3D perovskite structure by introducing layers of organic spacer moieties within the 3D structure, to form a layered 2D perovskite structure.^[14,15] The general formula for the 2D perovskite systems is S_xA_{n-1}B_nX_{3n+1}, where x depends on the number of large alkylammonium cations in the layer (x mostly equals 1 or 2), whereas n defines the number of perovskite slabs separated by the organic layer ($n = 1, 2, 3$, etc.; Figure 1c).^[13,14,16,17] Spacers are large organic alkylammonium cations that can be either mono- ($x = 2$) or bifunctional ($x = 1$) to produce 2D-perovskite Ruddlesden-Popper (RP) or Dion-Jacobson (DJ) phases.^[13,17–21] The electrical and optical properties of materials strongly depend on the number of 3D perovskite slabs (n) separated by the 2D layers, which are mainly comprised of insulating organic moieties.^[22] Therefore, these systems are highly anisotropic and the effective charge extraction depends on the orientation of the layers with respect to the selective charge-extraction layers.^[12,23]

This limitation stimulated the appearance of another approach that involves forming 2D/3D perovskite composites of 3D perovskite compositions with 2D overlayers, which show good photovoltaic performance with improvement in their operational stability.^[24–29] In this regard, 2-phenylethylammonium (PEA) has been particularly effective (Figure 2a).^[30–33] It has been shown that phenylalkylammonium analogues, e.g., benzylamine and aniline, can impart the formamidinium (FA) lead iodide film surface with improved electronic properties and moisture resistance.^[34] The remarkable optoelectronic properties of α -FAPbI₃ and its high thermal stability render it an ideal candidate for hybrid perovskite photovoltaics.^[35–36] However, under ambient temperature conditions, α -FAPbI₃ perovskite converts to the non-perovskite δ -phase that is not suitable for photovoltaics and stabilizing it without compromising the optoelectronic properties as well as device performances is an ongoing challenge.^[36] The use of phenylammonium analogues on the surface of FA_{0.9}Cs_{0.1}PbI_{2.9}Br_{0.1} films shows promise for suppressing hysteresis effects,^[36] whereas benzylammonium (Bz; Figure 2b) gave promising results,^[35–36] although its role in perovskite solar cells remain elusive.

Herein, we demonstrate stabilization of the α -FAPbI₃ phase by modifying it with benzylammonium (Bz) cations. Benzylamine features a delocalized π -system^[37,38] extending over the entire molecule, as shown by the density functional theory calculations^[39] which could contribute to lowering the barrier for charge-carrier transport as compared to other phenyl analogs. Moreover, the Bz features strong hydrophobicity^[34] and rigidity, without compromising the adaptability of the ammonium termini for binding to the perovskite surface.^[40,41] This could further direct the assembly of Bz moieties on the surface of α -FAPbI₃,^[42] while maintaining its optoelectronic properties.^[28] We reveal that BzI can interact with α -FAPbI₃ at the atomic level through hydrogen bonding, as evidenced by solid-state NMR spectroscopy, stabilizing it against the detrimental α -to- δ phase transition. Furthermore, adding BzI to the perovskite precursor (abbreviated as FAPbI₃(BzI)_x) leads to superior device performance and operational stability, as well as shelf-life over one year under ambient conditions.

2. Results and Discussion

We prepared hybrid perovskite films by dissolving the FAI, PbI₂, and BzI precursors in a mixture of *N,N*-dimethylformamide (DMF) and dimethyl sulfoxide (DMSO) of 4:1 volume ratio and depositing the precursor solution by spin coating it onto the electron selective contact with the layered architecture (mesoscopic(mp)/compact(c)TiO₂/fluorine-doped tin oxide (FTO) glass; Figure 1a). The details of the procedure are given in the Experimental Section.

The structural properties of the films are analyzed by X-ray diffraction (XRD) for different FAPbI₃(BzI)_x compositions ($x = 0, 0.05, 0.10, 0.25$, and 0.50). The films containing Bz moieties show patterns comparable to the 3D FAPbI₃ perovskite (Figure 2c). While the propensity of Bz to form a pure 2D Bz₂PbI₄ perovskite is evidenced by XRD (Figure S1, Supporting Information), there are no additional peaks observed in the lower angle domain ($2\theta < 10^\circ$) for FAPbI₃(BzI)_x which suggests

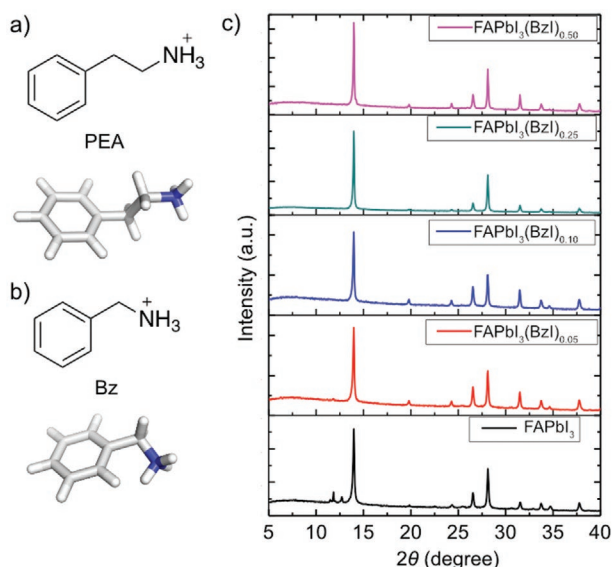


Figure 2. a,b) Structural representation of (a) commonly employed 2-phenylethylammonium (PEA) organic spacers for 2D perovskites and (b) benzylammonium (Bz) organic moieties employed in this study with the corresponding DFT-optimized structures (at the B3LYP 6–31G(d) level of theory).^[45] c) XRD patterns of the FAPbI₃(BzI)_x perovskite films.

the absence of low-dimensional perovskite phases under these conditions.^[17] Moreover, the film of FAPbI₃(BzI)_{0.25} does not show the presence of diffraction peaks associated with Bz₂PbI₄, as reported previously.^[43] In this earlier report, however, a strong reflection signal has been observed at 6.26°, which is not apparent for the films containing FAI. This suggests that the 2D phase either does not form in the presence of FAI or that it is highly disordered which prevents its detection. Alternatively, multiple low-dimensional phases of various mixed Bz/FA 2D/3D phases are likely to form, which could co-exist in lower concentrations and possibly feature lower level of crystallinity, leading to the disappearance of the low angle reflection peaks or their appearance in a different 2θ range. Nevertheless, other spectral signatures suggest presence of the interaction with the FAPbI₃. Specifically, while neat FAPbI₃ films contain δ-FAPbI₃

(2θ = 11.8°) and PbI₂ (2θ = 12.6°),^[40,43,44] these phases are absent in the films containing Bz, particularly for x > 0.05 compositions. This suggests that Bz affects the structure of FAPbI₃, which could be the result of surface modification or the formation of mixed low-dimensional Bz/FA phases.^[42]

This interaction was further assessed at the atomic-level by means of solid-state NMR spectroscopy. It has been shown that the solid-state NMR methods can be employed to investigate phase-segregation,^[46–49] cation-incorporation,^[50] cation-dynamics,^[51–53] halide mixing,^[48] and atomic-level proximities among various functional groups.^[54] ¹H-¹³C cross-polarization experiments were performed on neat BzI and FAPbI₃(BzI)_{0.25} samples (Figure 3, left) prepared by mechanosynthesis in accordance with the reported procedures.^[46–49] The NMR spectra of α-FAPbI₃ and δ-FAPbI₃ show distinguishable ¹³C resonances at 155.9 and 156.8 ppm, respectively (Figure 3a,b), while neat BzI shows aliphatic ¹³C resonances at 43.3 ppm and six aromatic resonances in the 125–136 ppm range (Figure 3c). In FAPbI₃(BzI)_{0.25}, the FA environments appear at 155.9 ppm evidencing the stabilization of the α-FAPbI₃ phase. Moreover, the aliphatic (40–50 ppm) and aromatic (125–136 ppm) signals of Bz are shifted compared to neat BzI, indicating that BzI has fully reacted with FAPbI₃ (Figure 3d). We initially assumed that this reaction might result in the formation of low-dimensional Bz₂FA_{n–1}Pb_nI_{3n+1} phases (with n = 1, 2, 3, ...) co-existing with the 3D FAPbI₃ perovskite phase. This would require the release of FAI as one of the side-products, which is known to be more volatile and/or act as a passivation agent.

Grazing-incidence wide-angle X-ray scattering (GIWAXS) measurements of n = 1–3 compositions, however, could not detect these in co-existence with the 3D perovskite within the FAPbI₃(BzI)_{0.25} composition, despite the capacity of BzI to form low-dimensional phases (Figures S2 and S3, Supporting Information). Instead, it shows a predominant formation of the 3D FAPbI₃ perovskite phase, suggesting its role as a molecular modulator at the surface and grain boundaries of FAPbI₃. This stabilization is in keeping with the previous reports on the structure-directing role of molecular modulators that template the α-FAPbI₃ phase and alter the energy landscape for the interconversion to the δ phase, hence stabilizing it.^[55–57]

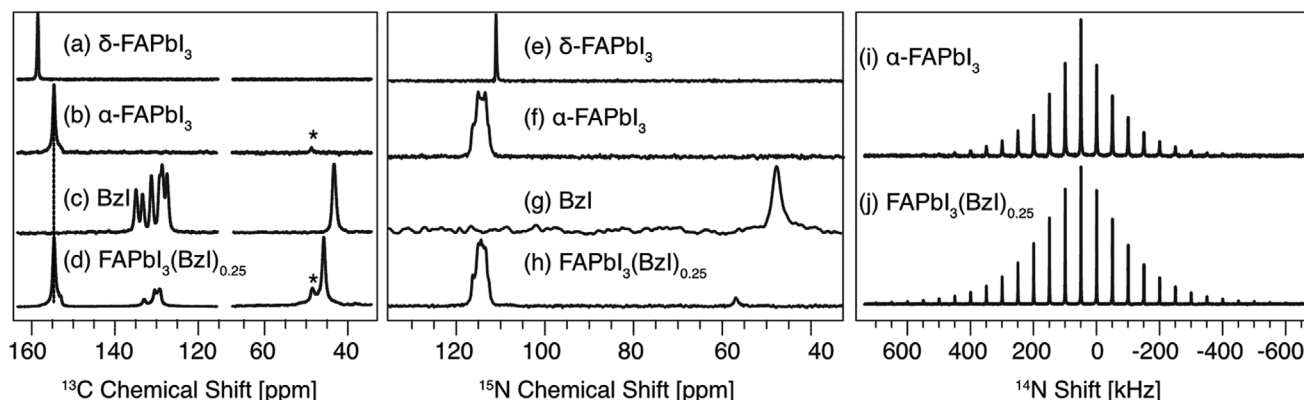


Figure 3. ¹H-¹³C cross-polarization (CP) with 12 kHz magic-angle spinning (MAS) at 100 K and 21.1 T of bulk microcrystalline a) δ-FAPbI₃, b) α-FAPbI₃, c) BzI, and d) FAPbI₃(BzI)_{0.25}. ¹H-¹⁵N cross-polarization (CP) with 12 kHz magic-angle spinning (MAS) at 100 K e) δ-FAPbI₃, f) α-FAPbI₃, g) BzI, and h) FAPbI₃(BzI)_{0.25}. ¹⁴N MAS NMR at 5 kHz MAS, 298 K and 21.1 T of i) α-FAPbI₃ and j) FAPbI₃(BzI)_{0.25}.

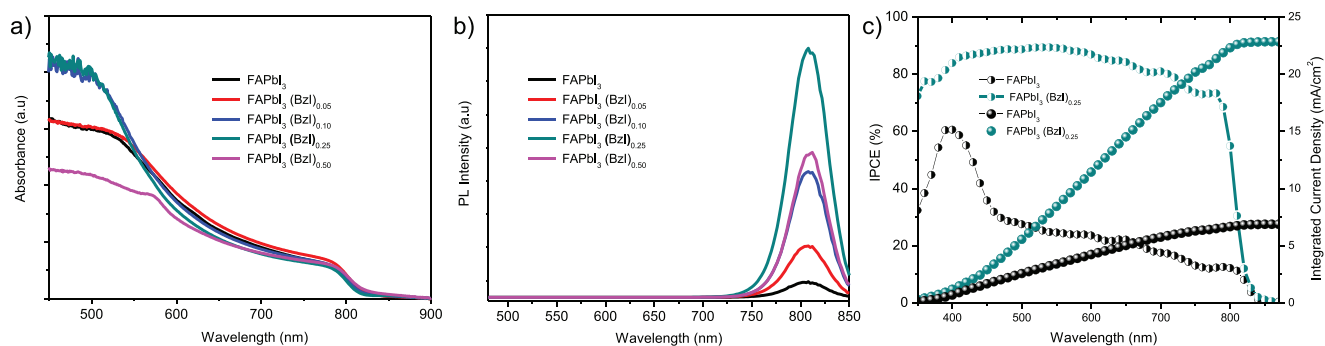


Figure 4. Characterization of the $\text{FAPbI}_3(\text{BzI})_x$ perovskite films of various compositions (x). a) UV-vis absorption, b) photoluminescence, and c) IPCE spectra (half spherical point; left Y-axis) with the integrated J_{sc} (full spherical point; right Y-axis) of the $\alpha\text{-FAPbI}_3$ and $\text{FAPbI}_3(\text{BzI})_{0.25}$ devices.

To further corroborate the atomic-level FA/Bz mixing, we performed low-temperature $^1\text{H}\text{-}^{15}\text{N}$ cross-polarization (CP) measurements (Figure 3e–h), which reveal the local chemical environment of the $-\text{NH}_3$ moieties in BzI and FA. $\delta\text{-FAPbI}_3$, $\alpha\text{-FAPbI}_3$ and BzI show well-resolved ^{15}N resonances at 111.0, 114.2, and 47.9 ppm, respectively. In BzI-doped FAPbI_3 , the BzI signal (56.9 ppm) is significantly shifted compared to neat BzI. This is accompanied by a change in the lineshape of the signal corresponding to the 3D FA environments, which suggests that the local structure of the perovskite phase is modified by the reaction with BzI (Figure 3h). This further corroborates the formation of a mixed Bz/FA phase which we identify as the direct reason for the observed stabilization effects. The Bz/FA interaction may also affect the symmetry of the cuboctahedral cavity, which we in turn probe using ^{14}N NMR spectroscopy. ^{14}N spectra of hybrid perovskites provide complementary insights into crystallographic changes on the local level owing to their sensitivity to the symmetry around the fast-reorienting A-site cation.^[28,57] Specifically, ^{14}N magic angle spinning (MAS) NMR spectra feature a spinning sideband (SSB) manifold whose width is highly sensitive to the symmetry of the local environment. ^{14}N MAS NMR of $\text{FAPbI}_3(\text{BzI})_{0.25}$ exhibits full width at half maximum (FWHM) of 120 kHz (Figure 3j), which is broader compared to $\alpha\text{-FAPbI}_3$ with FWHM of 70 kHz (Figure 3i), suggesting that the presence of BzI perturbs the symmetry of the cuboctahedral cavity, making it less cubic compared to the pristine $\alpha\text{-FAPbI}_3$.

We further analyzed the effect of BzI addition on the morphology of the FAPbI_3 films by means of scanning electron microscopy (SEM; Figure S4, Supporting Information). The changes in the morphology are apparent as the films based on the $x = 0.10$ composition appear smoother, while those of the $x = 0.25$ and 0.5 compositions show more surface roughness. This roughness can contribute to an increase of the contact area with the hole transporting material in the resulting device. In addition, the effect of BzI on the thickness is apparent via the cross-sectional images of FAPbI_3 and $\text{FAPbI}_3(\text{BzI})_{0.25}$ layers (Figure S4, Supporting Information), showing a slight difference in thicknesses, which can be attributed to the changes in the grain size of the $\text{FAPbI}_3(\text{BzI})_{0.25}$ film. The effect of BzI moieties on the optical properties was also apparent, as shown by UV-vis absorption spectroscopy (Figure 4a). While UV-vis absorption spectra of the control and the films containing 25% BzI exhibit no change in the absorption edge, there is an increase in the absorbance in the spectral range below 600 nm

(Figure S5a, Supporting Information). There are no clear indicators of the presence of Bz_2PbI_4 phase in the absorption spectra. Specifically, the absorption spectra of the films based on $\text{FAPbI}_3(\text{BzI})_{0.25}$ composition show an onset at 830 nm, which suggests that the presence of BzI at this quantity does not compromise the optoelectronic properties of FAPbI_3 . Moreover, steady state photoluminescence (PL) spectra for neat FAPbI_3 and $\text{FAPbI}_3(\text{BzI})_x$ films show maximum emission peaks at 810 nm consistent with the 3D FAPbI_3 phase (Figure 4b) without clear evidence for the presence of the $(\text{Bz})_2\text{PbI}_4$ phase in the $\text{FAPbI}_3(\text{BzI})_{0.25}$ film (Figure S5b, Supporting Information).^[58,59] The incident photon-to-current conversion efficiency (IPCE) spectra of $\alpha\text{-FAPbI}_3$ and $\alpha\text{-FAPbI}_3(\text{BzI})_{0.25}$ (Figure 4c) match the absorption edge of the photocurrent for the control and champion $\alpha\text{-FAPbI}_3(\text{BzI})_{0.25}$ -containing perovskite devices in the fluorine doped tin oxide (FTO)/compact (c) $\text{TiO}_2/\text{mesoporous (mp) TiO}_2/\text{perovskite}/2,2',7,7'\text{-tetrakis-(N,N-di-4-methoxyphenylamino)-9,9'-spirobifluorene (spiro-OMeTAD)}/\text{Au}$ architecture. The IPCE increases up to 60% around 400 nm and decreases to 10% at 800 nm for neat FAPbI_3 , presumably due to the existence of the δ phase. On the contrary, the IPCE retains about 80% for $\text{FAPbI}_3(\text{BzI})_{0.25}$ throughout the entire spectral range between 400 and 830 nm, which highlights the stabilization effect that is particularly relevant for the photovoltaic performance.

Photovoltaic performance was analyzed for devices based on $\text{FAPbI}_3(\text{BzI})_x$ ($x = 0, 0.05, 0.10, 0.25$, and 0.50) compositions by employing FTO/c- $\text{TiO}_2/\text{mp-TiO}_2/\text{perovskite}/\text{spiro-OMeTAD}/\text{Au}$ device architecture and extracting the corresponding photovoltaic parameters under simulated 1.5 sunlight and a $J\text{-}V$ scan rate of 40 mV s^{-1} (Figure 5). The control devices containing neat FAPbI_3 ($x = 0$) show a poor performance with a maximum power conversion efficiency (PCE) of 6.97%, open circuit voltage (V_{oc}) of 0.88 V, short circuit current density (J_{sc}) of 17.84 mA cm^{-2} , and a fill factor (FF) of 0.55 (Figure S6a, Supporting Information). The device performance gradually improves with the increase of the Bz ratio from 5% to 25%, after which it declines with further increase of the BzI content. This decline in performance can be attributed to the insulating character of the organic moieties that would result in poor conductivity for higher BzI quantities. The champion device based on the 25% BzI achieved a maximum PCE of 20.2% with a V_{oc} of 1.1 V, J_{sc} of 25 mA cm^{-2} , and FF of 73% (Figure S6b, Supporting Information). The presence of BzI affects also the

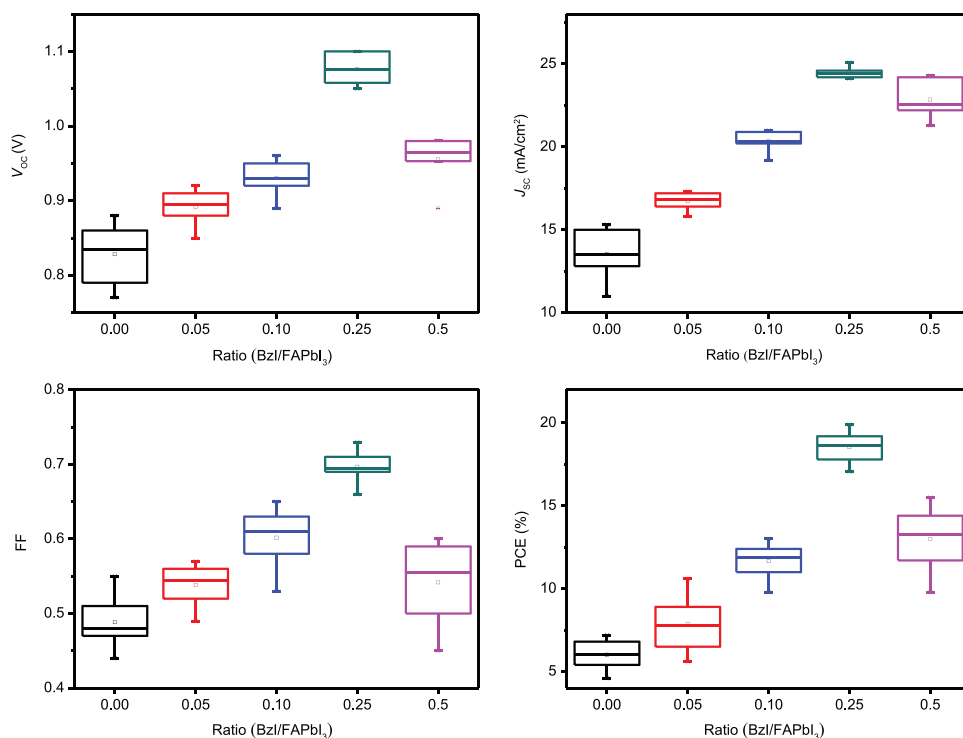


Figure 5. Photovoltaic parameters for 20 devices based on FAPbI₃(BzI)_x (x = 0, 0.05, 0.10, 0.25, and 0.50) perovskite composition.

hysteresis in the J - V curves, which was probed by J - V scans with a rate of 40 mV s⁻¹ for FAPbI₃ and FAPbI₃(BzI)_{0.25} devices (Figure S6c,d: Supporting Information). The data reveal lower hysteresis for the FAPbI₃(BzI)_{0.25} compositions in comparison with the control.

To determine the origin of the V_{OC} and FF increase observed with the BzI treated devices, we carried out steady-state photoluminescence quantum yield (PLQY) and time-resolved photoluminescence (TRPL) measurements (Figure 6). PLQY was determined by absolute PL spectral photon flux measurements at one sun condition using an integrating sphere (Figure 6a).^[60] The BzI-treated device shows an order of magnitude higher PLQY than the untreated device. A PLQY < 1 translates into a voltage loss due to non-radiative recombination of $\Delta V = -k_B T/q \ln(\text{PLQY})$ and a quasi-Fermi level splitting ΔE_F of $\Delta E_F = V_{OC,SQ} + \Delta V$, where k_B is the Boltzmann constant, $T = 25$ °C the sample temperature, q the elementary charge and $V_{OC,SQ}$ the Shockley-Queisser limit of V_{OC} .^[61] $\Delta E_F/q$ is the internal voltage of the absorber layer, which represents the maximum obtainable V_{OC} of a device with this absorber.

If we compare ΔE_F with the stabilized V_{OC} measured with the same device (Figure 6b) we observe that both follow the same trend. The mismatch between these two quantities originates from the combination of energy level misalignments at the perovskite/TiO₂ and perovskite/spiro-OMeTAD interface in combination with radiationless interfacial charge carrier recombination.^[62] These findings show that the increase in V_{OC} can be attributed to suppressed trap-assisted non-radiative recombination which demonstrates the beneficial effect of the BzI modulation on the defect chemistry. Since non-radiative

recombination lower the FF,^[63] this also explains in part the FF increase of the BzI-modulated FAPbI₃ device.

Furthermore, the TRPL traces of neat FAPbI₃ and (BzI)_{0.25} FAPbI₃ samples with mp-TiO₂ but without HTM (Figure 6c) reveal two features, a fast decay within the first 50–100 ns followed by a slower mono-exponential decay. The fast decay at early times is dominated by charge transfer from the perovskite film into TiO₂^[64] whereas the later decay is mainly caused by non-radiative bulk, interface or surface recombination of the perovskite film. The BzI treatment leads to a faster electron transfer into the ETL and to 25 times longer carrier lifetime (τ). Assuming that these lifetimes are dominated by bulk recombination, the measured τ values yield a non-radiative monomolecular (SRH) recombination constant $k_1 = 1/(2\tau)$ of 5.3×10^6 s⁻¹ for the neat and 2.0×10^5 s⁻¹ for the BzI-modulated perovskite film. This further demonstrates the beneficial effect of BzI on the defect chemistry of the FAPbI₃ film and is in good agreement with the improvement in the V_{OC} and FF. To investigate the effect of the BzI modulation on hole transport into the HTL, we measured TRPL on samples with spiro-OMeTAD (Figure 6d). In this case, the fast-initial decay within the first 50 ns is again dominated by charge transfer. The faster PL decay for the BzI-modulated film shows its beneficial effect on the hole transfer into the HTL. As a result, BzI treatment leads to a faster electron and hole transfer which is further contributing to an increase in FF.

Moreover, the maximum power point (MPP) tracking of the FAPbI₃(BzI)_{0.25} device shows a stable PCE of 20.0% after 300 s of constant 1.5 AM illumination (Figure S6e, Supporting Information), indicating stabilization of the maximum power output. We have also monitored the shelf-stability of the devices during

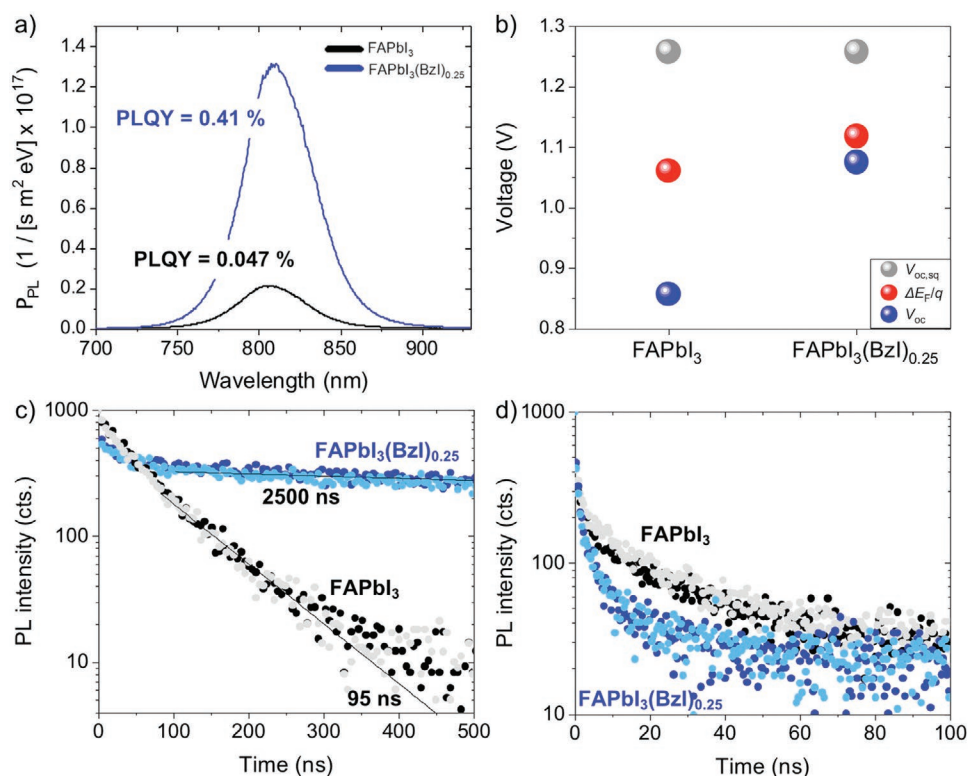


Figure 6. a) Absolute PL spectral photon flux measurements of complete solar cell devices using FAPbI₃ and (BzI)_{0.25}FAPbI₃. b) Quasi-Fermi level splitting ΔE_F determined from PLQY of the devices in (a). Shown are also the Shockley-Queisser limit of V_{OC} ($V_{OC, SQ}$) and the measured V_{OC} of the same devices. (c) Time-resolved PL traces for the neat FAPbI₃ and (BzI)_{0.25}FAPbI₃ samples with the architecture FTO/c-TiO₂/mp-TiO₂/perovskite. Shown are the traces of two independent samples for each condition (circles) and mono-exponential fit curves (black lines) with the respective lifetimes. All measured curves start at 1000 cts. d) Same measurements as in (c) but with spiro-OMeTAD on top of the perovskite layer.

one year under ambient conditions and we measured the $J-V$ for two unencapsulated devices of FAPbI₃ and FAPbI₃(BzI)_{0.25}. The control devices based on FAPbI₃ showed a rapid decline in performance, whereas devices based on the FAPbI₃(BzI)_{0.25} composition maintain 80% of the initial PCE over one year under ambient (shelf-life) conditions (Figure 7a). The effects of these structural properties on the long-term operational stability were further probed under continuous AM1.5G irradiation (100 mW cm⁻²) and maximum power point tracking in a nitrogen atmosphere at room temperature (Figure 7b). The comparison of the neat FAPbI₃ and FAPbI₃(BzI)_{0.25}-based PSC shows that the operational stability of the FAPbI₃(BzI)_{0.25}-based device is greatly improved, retaining 85% of its initial PCE up to 140 h. On the contrary, the PCE of neat α -FAPbI₃ device declines rapidly and reaches 10% of its initial efficiency within 100 h. This highlights the potential of this approach in achieving PSCs with long-term stability.

3. Conclusion

In summary, we have demonstrated that the addition of benzylammonium (Bz) iodide results in the stabilization of the black perovskite α -FAPbI₃ phase. The microscopic effects of the additive have been elucidated using multi-nuclear solid-state NMR spectroscopy complemented by X-ray scattering measurements. We show that Bz reacts with α -FAPbI₃

to render α -FAPbI₃ more stable. In this phase, the Bz moieties modulate the surface of the FAPbI₃ and grain boundaries without forming low-dimensional perovskite phases. This modulation strategy strongly enhances the optoelectronic quality of the perovskite phase as has been shown by PLQY and TRPL measurements. As a result, perovskite solar cells based on FAPbI₃(BzI)_{0.25} show power conversion efficiencies exceeding 20% and superior stability, maintaining 80% of the initial PCE after one year under ambient shelf-life conditions. This strategy thus provides a new way of stabilizing the black (α) perovskite phase of FAPbI₃ in perovskite solar cells.

4. Experimental Section

Materials: All materials were purchased from Sigma-Aldrich and used as received, unless stated otherwise. Perovskite powders for solid-state NMR studies were synthesized by grinding precursors in an electric ball mill (Retsch Ball Mill MM-200, grinding jar with a volume of 10 mL and 1 agate ball, diameter size 10 mm) for 30 min at 25 Hz. The precursors were packed in a glove box under an argon atmosphere. After milling, the resulted powders were annealed at 140 °C for 10 min to remove grinding-induced defects. The following amounts of reagents were used: FAPbI₃: 0.172 g FAI (1 mmol) and 0.461 g PbI₂ (1 mmol); FAPbI₃(BzI)_{0.25}: 0.172 g FAI (1 mmol) and 0.461 g PbI₂ (1 mmol) and 0.029 g BzI (0.25 mmol).

Solar Cell Preparation: Fluorine-doped tin oxide (FTO)-glass substrates (TCO glass, NSG 10, Nippon sheet glass, Japan) were etched from the edges by using Zn powder and 4 M HCl and then, were cleaned by ultrasonication in Hellmanex (2%, deionized water),

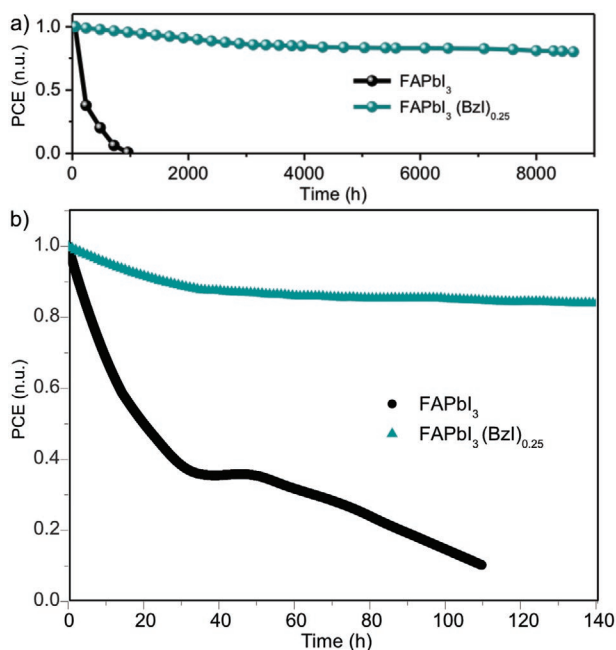


Figure 7. a) Average shelf stability by monitoring the evolution of performance of the corresponding non-encapsulated solar cells exposed to the ambient environment with relative 40% humidity in the dark at ambient temperature (n.u. = normalized units with respect to the initial performance). Initial PCE = 20%. b) Normalized PCE of neat FAPbI₃ and (Bzl)_{0.25} FAPbI₃ based devices monitored under continuous white light exposure in the Nitrogen atmosphere, at 25 °C, as a function of time (140 h). Initial PCE = 19%.

rinsed thoroughly with de-ionized water and ethanol, and then treated in oxygen plasma for 15 min. A 30 nm blocking layer (TiO₂) was deposited on the cleaned FTO by spray pyrolysis at 450 °C using a commercial titanium diisopropoxide bis(acetylacetonate) solution (75% in 2-propanol, Sigma-Aldrich) diluted in anhydrous ethanol (1:9 volume ratio) as precursor and oxygen as a carrier gas. A mesoporous TiO₂ layer was deposited by spin-coating a diluted paste (1:6 wt ratio) (Dyesol 30NRD: ethanol) (4000 rpm, acceleration 2000 rpm for 20 s) onto the substrate containing a TiO₂ compact layer, and then sintered at 450 °C for 30 min in dry air.

Deposition of Perovskite Films: The perovskite films were deposited using a single-step deposition method from the precursor solution. The precursor solution of FAPbI₃ was prepared in Argon atmosphere by dissolving equimolar amounts of PbI₂ and FAI in an anhydrous DMF/DMSO (4:1 (volume ratio)) mixture at a concentration of 1.3 M. Next, benzylammonium iodide (Bzl) was added into the FAPbI₃ precursor solution using different molar ratios, resulting in several FAPbI₃(Bzl)_x compositions (x = 0.05, 0.10, 0.25, and 0.50). The device fabrication was carried out under controlled atmospheric conditions with humidity <2%. The precursor solution was spin-coated onto the mesoporous TiO₂ films in a one-step program at 600 and 5000 rpm for 30 s. 200 μL of chlorobenzene was dropped on the spinning substrate 10 s prior the end of the program. This was followed by annealing the films at 150 °C for 30–40 min. After preparing the initial perovskite layer (control) as described above, the film was cooled down at room temperature. For completing the fabrication of devices, 90 mg of 2,2',7,7'-tetrakis(N,N-di-p-methoxyphenylamine)-9,9-spirobifluorene (spiro-OMeTAD) was dissolved in 1 mL of chlorobenzene as a hole-transporting material. The HTM was deposited by spin-coating at 4000 rpm for 20 s. The HTM was doped with bis(trifluoromethylsulfonyl) imide lithium salt (17.8 μL prepared by dissolving 520 mg LiTFSI in 1 mL of acetonitrile), and 28.8 μL of 4-tert-butylpyridine. Finally, a ≈80 nm gold (Au) layer was thermally evaporated.

Device Characterization: The current–voltage (J–V) characteristics of the perovskite devices were recorded with a digital source meter (Keithley model 2400, USA). A 450 W xenon lamp (Oriol, USA) was used as the light source for photovoltaic (J–V) measurements. The spectral output of the lamp was filtered using a Schott K113 Tempax sunlight filter (Präzisions Glas & Optik GmbH, Germany) to reduce the mismatch between the simulated and actual solar spectrum to less than 2%. The photo-active area of 0.16 cm² was defined using a dark-colored metal mask.

Incident Photon-to-Current Efficiency (IPCE): IPCE was recorded under a constant white light bias of ≈5 mW cm⁻² supplied by an array of white light emitting diodes. The excitation beam coming from a 300 W Xenon lamp (ILC Technology) was focused through a Gemini-180 double monochromator (Jobin Yvon Ltd) and chopped at ≈2 Hz. The signal was recorded using a Model SR830 DSP Lock-In Amplifier (Stanford Research Systems).

Photoluminescence Quantum Yield: Photoluminescence quantum yield was measured using an integrating sphere (Gigahertz-Optik, an Andor Kymera 193i spectrograph and a 660 nm continuous-wave laser (OBIS, Coherent) set at 1 Sun equivalent photon flux (790 μm beam full-width half-maximum, 330 μW); the photoluminescence signal was collected at normal incidence using an optical fiber. For the calibration of the PLQY measurements a halogen lamp (BN-LH250-V01, Gigahertz-Optik) was used, to proof the correctness of the calibration PLQY of a dye solution of indocyanine green was measured in DMSO in the same setup and PLQY values were measured within 15% deviation from the literature values.

Time-Resolved Photoluminescent (TRPL): TRPL was measured via time-correlated single photon counting (TCSPC) using a LifeSpec II (Edinburgh Instruments) fluorescence spectrometer with a picosecond pulsed diode laser (EPL-510, Edinburgh Instruments) at 510 nm wavelength and 85 ps pulse width. The laser fluence used was 5 nJ cm⁻².

Scanning Electron microscopy (SEM): SEM was performed on a ZEISS Merlin HR-SEM.

X-Ray Powder Diffractions: X-ray powder diffraction was recorded on an X'Pert MPD PRO (Panalytical) equipped with a ceramic tube (Cu anode, λ = 1.54060 Å), a secondary graphite (002) monochromator and a RTMS X'Celerator (Panalytical).

Grazing Incidence Wide Angle X-Ray Scattering: Grazing incidence wide angle X-ray scattering was measured on a xenocs XEUSS 2.0 laboratory beamline under a pressure of 0.1 bar, using Cu K_α radiation and incident angles below 0.5°.

UV–Vis Measurements: UV–vis measurements were performed on a Varian Cary 5.

NMR Spectroscopy: NMR spectroscopy involved low-temperature ¹³C (225 MHz), ¹⁵N (90.23 MHz) and room-temperature ¹⁴N (65 MHz) NMR spectra were recorded on a Bruker Avance Neo 21.1 T spectrometer equipped with a 3.2 mm low-temperature CPMAS probe. ¹³C chemical shifts were referenced to solid adamantane [δ_C = 29.45 (CH) and 38.48 (CH₂) ppm]. ¹⁴N and ¹⁵N chemical shift were referenced to solid NH₄Cl with shift at 0 and 39 ppm. Low-temperature ¹H–¹³C CP experiments used 1 ms optimized contact pulses, SPINAL-64 ¹H decoupling, and the following recycle delays: 1.7 s (δ-FAPbI₃), 4 s (α-FAPbI₃), 1000 s (Bzl), 5 s (FAPbI₃(Bzl)_{0.25}). Low-temperature ¹H–¹⁵N CP experiments used 1 ms optimized contact pulses, SPINAL-64 ¹H decoupling, and the following recycle delays: 1.7 s (δ-FAPbI₃), 3 s (α-FAPbI₃), 1000 s (Bzl), 5 s (FAPbI₃(Bzl)_{0.25}). Peak widths were fitted in Topspin 3.6.0 and the uncertainties are given at one standard deviation.

Supporting Information

Supporting Information is available from the Wiley Online Library or from the author.

Acknowledgements

M.G. and S.M.Z. thank the King Abdulaziz City for Science and Technology (KACST) for financial support. A.Q.A. and M.H.A. gratefully

acknowledge KACST for the fellowship. H.Z. thanks the financial support from the European Union's Horizon 2020 research and innovation programme under grant agreement No. 881603. J.V.M. is grateful for the Swiss National Science Foundation grant no. 193174. L.M., A.H., F.S. gratefully acknowledge funding by the DFG (SPP 2196) No. SCHR 700/38-1. The authors are grateful to Thomas Schneeberger for designing the schematic representing perovskite solar cells. D.J.K. is presently affiliated with the University of Cambridge, Cavendish Laboratory, J J Thomson Avenue, Cambridge CB3 0HE, United Kingdom. J.V.M. is presently affiliated with the Adolphe Merkle Institute of the University of Fribourg in Switzerland.

Conflict of Interest

The authors declare no conflict of interest.

Data Availability Statement

The data that support the findings of this study are openly available on Zenodo at <https://doi.org/10.5281/zenodo.4752189>.

Keywords

benzylammonium, formamidinium lead iodide, low-dimensional perovskites, solid-state NMR

Received: February 3, 2021

Revised: March 26, 2021

Published online: May 19, 2021

- [1] A. Kojima, K. Teshima, Y. Shirai, T. Miyasaka, *J. Am. Chem. Soc.* **2009**, *131*, 6050.
- [2] National Renewable Energy Laboratory (NREL), <https://www.nrel.gov/pv/cell-efficiency.html> (accessed: May 2020).
- [3] M. Luan, J. Song, X. Wei, F. Chen, J. Liu, *CrystEngComm* **2016**, *18*, 5257.
- [4] S. P. Singh, P. Nagarjuna, *Dalton Trans.* **2014**, *43*, 5247.
- [5] C. C. Stoumpos, C. D. Malliakas, M. G. Kanatzidis, *Inorg. Chem.* **2013**, *52*, 9019.
- [6] T. Baikie, Y. Fang, J. M. Kadro, M. Schreyer, F. Wei, S. G. Mhaisalkar, M. Graetzel, T. J. White, *J. Mater. Chem. A* **2013**, *1*, 5628.
- [7] M. A. Green, A. Ho-Baillie, H. J. Snaith, *Nat. Photonics* **2014**, *8*, 506.
- [8] S. Sun, T. Salim, N. Mathews, M. Duchamp, C. Boothroyd, G. Xing, T. C. Sum, Y. M. Lam, *Energy Environ. Sci.* **2014**, *7*, 399.
- [9] A. K. Jena, A. Kulkarni, T. Miyasaka, *Chem. Rev.* **2019**, *119*, 3036.
- [10] A. Amat, E. Mosconi, E. Ronca, C. Quarti, P. Umari, M. d. K. Nazeeruddin, M. Grätzel, F. De Angelis, *Nano Lett.* **2014**, *14*, 3608.
- [11] W.-F. Yang, F. Igbari, Y.-H. Lou, Z.-K. Wang, L.-S. Liao, *Adv. Energy Mater.* **2019**, *10*, 1902584.
- [12] G. Grancini, M. K. Nazeeruddin, *Nat. Rev. Mater.* **2019**, *4*, 4.
- [13] L. Mao, C. C. Stoumpos, M. G. Kanatzidis, *J. Am. Chem. Soc.* **2019**, *141*, 1171.
- [14] B. Saparov, D. B. Mitzi, *Chem. Rev.* **2016**, *116*, 4558.
- [15] A. Krishna, S. Gottis, M. K. Nazeeruddin, F. Sauvage, *Adv. Funct. Mater.* **2019**, *29*, 1806482.
- [16] D. H. Cao, C. C. Stoumpos, O. K. Farha, J. T. Hupp, M. G. Kanatzidis, *J. Am. Chem. Soc.* **2015**, *137*, 7843.
- [17] C. C. Stoumpos, D. H. Cao, D. J. Clark, J. Young, J. M. Rondinelli, J. I. Jang, J. T. Hupp, M. G. Kanatzidis, *Chem. Mater.* **2016**, *28*, 2852.
- [18] L. Mao, W. Ke, L. Pedesseau, Y. Wu, C. Katan, J. Even, M. R. Wasielewski, C. C. Stoumpos, M. G. Kanatzidis, *J. Am. Chem. Soc.* **2018**, *140*, 3775.
- [19] X. Li, J. Hoffman, W. Ke, M. Chen, H. Tsai, W. Nie, A. D. Mohite, M. Kepenekian, C. Katan, J. Even, M. R. Wasielewski, C. C. Stoumpos, M. G. Kanatzidis, *J. Am. Chem. Soc.* **2018**, *140*, 12226.
- [20] W. Ke, L. Mao, C. C. Stoumpos, J. Hoffman, I. Spanopoulos, A. D. Mohite, M. G. Kanatzidis, *Adv. Energy Mater.* **2019**, *9*, 1803384.
- [21] Y. Li, J. V. Milić, A. Ummadisingu, J.-Y. Seo, J.-H. Im, H.-S. Kim, Y. Liu, M. I. Dar, S. M. Zakeeruddin, P. Wang, A. Hagfeldt, M. Grätzel, *Nano Lett.* **2019**, *19*, 150.
- [22] J. Even, L. Pedesseau, C. Katan, *ChemPhysChem* **2014**, *15*, 3733.
- [23] H. Tsai, W. Nie, J.-C. Blancon, C. C. Stoumpos, C. M. M. Soe, J. Yoo, J. Crochet, S. Tretiak, J. Even, A. Sadhanala, G. Azzellino, R. Brenes, P. M. Ajayan, V. Bulović, S. D. Stranks, R. H. Friend, M. G. Kanatzidis, A. D. Mohite, *Adv. Mater.* **2018**, *30*, 1704217.
- [24] T. Niu, J. Lu, M.-C. Tang, D. Barrit, D.-M. Smilgies, Z. Yang, J. Li, Y. Fan, T. Luo, I. McCulloch, A. Amassian, S. (F.) Liu, K. Zhao, *Energy Environ. Sci.* **2018**, *11*, 3358.
- [25] Z. Wang, Q. Lin, F. P. Chmiel, N. Sakai, L. M. Herz, H. J. Snaith, *Nat. Energy* **2017**, *2*, 17135.
- [26] Y. Cho, A. M. Soufiani, J. S. Yun, J. Kim, D. S. Lee, J. Seidel, X. Deng, M. A. Green, S. Huang, A. W. Y. Ho-Baillie, *Adv. Energy Mater.* **2018**, *8*, 1703392.
- [27] Y. Liu, S. Akin, L. Pan, R. Uchida, N. Arora, J. V. Milić, A. Hinderhofer, F. Schreiber, A. R. Uhl, S. M. Zakeeruddin, A. Hagfeldt, M. I. Dar, M. Grätzel, *Sci. Adv.* **2019**, *5*, eaaw2543.
- [28] A. Q. Alanazi, D. J. Kubicki, D. Prochowicz, E. A. Alharbi, M. E. F. Bouduban, F. Jahanbakhshi, M. Mladenović, J. V. Milić, F. Giordano, D. Ren, A. Y. Alyamani, H. Albrithen, A. Albadri, M. H. Alotaibi, J.-E. Moser, S. M. Zakeeruddin, U. Rothlisberger, L. Emsley, M. Grätzel, *J. Am. Chem. Soc.* **2019**, *141*, 17659.
- [29] L. Hong, J. V. Milić, P. Ahlawat, M. Mladenović, D. J. Kubicki, F. Jahanbakhshi, D. Ren, M. C. Gélvez-Rueda, M. A. Ruiz-Preciado, A. Ummadisingu, Y. Liu, C. Tian, L. Pan, S. M. Zakeeruddin, A. Hagfeldt, F. C. Grozema, U. Rothlisberger, L. Emsley, H. Han, M. Graetzel, *Angew. Chem., Int. Ed.* **2020**, *59*, 4691.
- [30] A. H. Proppe, R. Quintero-Bermudez, H. Tan, O. Voznyy, S. O. Kelley, E. H. Sargent, *J. Am. Chem. Soc.* **2018**, *140*, 2890.
- [31] P. Chen, Y. Bai, S. Wang, M. Lyu, J.-H. Yun, L. Wang, *Adv. Funct. Mater.* **2018**, *28*, 1706923.
- [32] J. Qing, X.-K. Liu, M. Li, F. Liu, Z. Yuan, E. Tiukalova, Z. Yan, M. Duchamp, S. Chen, Y. Wang, S. Bai, J.-M. Liu, H. J. Snaith, C.-S. Lee, T. C. Sum, F. Gao, *Adv. Energy Mater.* **2018**, *8*, 1800185.
- [33] J. Qing, C. Kuang, H. Wang, Y. Wang, X.-K. Liu, S. Bai, M. Li, T. C. Sum, Z. Hu, W. Zhang, F. Gao, *Adv. Mater.* **2019**, *31*, 1904243.
- [34] F. Wang, W. Geng, Y. Zhou, H.-H. Fang, C.-J. Tong, M. A. Loi, L.-M. Liu, N. Zhao, *Adv. Mater.* **2016**, *28*, 9986.
- [35] H.-S. Yoo, N.-G. Park, *Sol. Energy Mater. Sol. Cells* **2018**, *179*, 57.
- [36] A. Binek, F. C. Hanusch, P. Docampo, T. Bein, *J. Phys. Chem. Lett.* **2015**, *6*, 1249.
- [37] Y.-J. Cheng, S.-H. Yang, C.-S. Hsu, *Chem. Rev.* **2009**, *109*, 5868.
- [38] T. Saitoh, T. Matsudo, C. Matsubara, *J. Chromatogr. A* **2000**, *879*, 121.
- [39] B.-E. Cohen, M. Wierzbowska, L. Etgar, *Sustainable Energy Fuels* **2017**, *1*, 1935.
- [40] Z. Cheng, J. Lin, *CrystEngComm* **2010**, *12*, 2646.
- [41] J. V. Milić, J.-H. Im, D. J. Kubicki, A. Ummadisingu, J.-Y. Seo, Y. Li, M. A. Ruiz-Preciado, M. I. Dar, S. M. Zakeeruddin, L. Emsley, M. Grätzel, *Adv. Energy Mater.* **2019**, *9*, 1900284.
- [42] Y. Fu, T. Wu, J. Wang, J. Zhai, M. J. Shearer, Y. Zhao, R. J. Hamers, E. Kan, K. Deng, X.-Y. Zhu, S. Jin, *Nano Lett.* **2017**, *17*, 4405.
- [43] S.-Y. Kim, J.-M. Yang, E.-S. Choi, N.-G. Park, *Nanoscale* **2019**, *11*, 14330.

- [44] Q. Han, S.-H. Bae, P. Sun, Y.-T. Hsieh, Y. (Michael) Yang, Y. S. Rim, H. Zhao, Q. Chen, W. Shi, G. Li, Y. Yang, *Adv. Mater.* **2016**, *28*, 2253.
- [45] a) J. B. Foresman, Æ. Frisch, in *Exploring Chemistry with Electronic Structure Methods*, 2nd ed., Gaussian, Inc., Pittsburgh, PA **1995**, pp. 1–335. b) Gaussian 16, Revision A.03, M. J. Frisch, G. W. Trucks, H. B. Schlegel, G. E. Scuseria, M. A. Robb, J. R. Cheeseman, G. Scalmani, V. Barone, G. A. Petersson, H. Nakatsuji, X. Li, M. Caricato, A. V. Marenich, J. Bloino, B. G. Janesko, R. Gomperts, B. Mennucci, H. P. Hratchian, J. V. Ortiz, A. F. Izmaylov, J. L. Sonnenberg, D. Williams-Young, F. Ding, F. Lipparini, F. Egidi, J. Goings, B. Peng, A. Petrone, T. Henderson, D. Ranasinghe, V. G. Zakrzewski, J. Gao, N. Rega, G. Zheng, W. Liang, M. Hada, M. Ehara, K. Toyota, R. Fukuda, J. Hasegawa, M. Ishida, T. Nakajima, Y. Honda, O. Kitao, H. Nakai, T. Vreven, K. Throssell, J. A. Montgomery Jr., J. E. Peralta, F. Ogliaro, M. J. Bearpark, J. J. Heyd, E. N. Brothers, K. N. Kudin, V. N. Staroverov, T. A. Keith, R. Kobayashi, J. Normand, K. Raghavachari, A. P. Rendell, J. C. Burant, S. S. Iyengar, J. Tomasi, M. Cossi, J. M. Millam, M. Klene, C. Adamo, R. Cammi, J. W. Ochterski, R. L. Martin, K. Morokuma, O. Farkas, J. B. Foresman, D. J. Fox, Gaussian, Inc. Wallingford CT **2016**.
- [46] D. J. Kubicki, D. Prochowicz, A. Hofstetter, S. M. Zakeeruddin, M. Grätzel, L. Emsley, *J. Am. Chem. Soc.* **2018**, *140*, 7232.
- [47] D. J. Kubicki, D. Prochowicz, A. Hofstetter, S. M. Zakeeruddin, M. Grätzel, L. Emsley, *J. Am. Chem. Soc.* **2017**, *139*, 14173.
- [48] B. A. Rosales, L. Men, S. D. Cady, M. P. Hanrahan, A. J. Rossini, J. Vela, *Chem. Mater.* **2016**, *28*, 6848.
- [49] A. Karmakar, M. S. Dodd, X. Zhang, M. S. Oakley, M. Klobukowski, V. K. Michaelis, *Chem. Commun.* **2019**, *55*, 5079.
- [50] J. Zhang, Z. Wang, A. Mishra, M. Grätzel, W. Guo, A. Hagfeldt, M. Yu, M. Shasti, W. Tress, D. Kubicki, C. Avalos, H. Lu, Y. Liu, B. Carlsen, A. Agarwalla, Z. Wang, W. Xiang, L. Emsley, Z. Zhang, *Joule* **2020**, *4*, 222.
- [51] G. M. Bernard, R. E. Wasylshen, C. I. Ratcliffe, V. Terskikh, Q. Wu, J. M. Buriak, T. Hauger, *J. Phys. Chem. A* **2018**, *122*, 1560.
- [52] R. E. Wasylshen, O. Knop, J. B. Macdonald, *Solid State Commun.* **1985**, *56*, 581.
- [53] D. J. Kubicki, D. Prochowicz, A. Hofstetter, P. Péchy, S. M. Zakeeruddin, M. Grätzel, L. Emsley, *J. Am. Chem. Soc.* **2017**, *139*, 10055.
- [54] E. A. Alharbi, A. Y. Alyamani, D. J. Kubicki, A. R. Uhl, B. J. Walder, A. Q. Alanazi, J. Luo, A. Burgos-Caminal, A. Albadri, H. Albrithen, M. H. Alotaibi, J.-E. Moser, S. M. Zakeeruddin, F. Giordano, L. Emsley, M. Grätzel, *Nat. Commun.* **2019**, *10*, 3008.
- [55] D. Bi, X. Li, J. V. Milić, D. J. Kubicki, N. Pellet, J. Luo, T. LaGrange, P. Mettraux, L. Emsley, S. M. Zakeeruddin, M. Grätzel, *Nat. Commun.* **2018**, *9*, 4482.
- [56] H. Lu, Y. Liu, P. Ahlawat, A. Mishra, W. R. Tress, F. T. Eickemeyer, Y. Yang, F. Fu, Z. Wang, C. E. Avalos, B. I. Carlsen, A. Agarwalla, X. Zhang, X. Li, Y. Zhan, S. M. Zakeeruddin, L. Emsley, U. Rothlisberger, L. Zheng, A. Hagfeldt, M. Grätzel, *Science* **2020**, *370*, eabb8985.
- [57] M. A. Ruiz-Preciado, D. J. Kubicki, A. Hofstetter, L. McGovern, M. H. Futscher, A. Ummadisingu, R. Gershoni-Poranne, S. M. Zakeeruddin, B. Ehrler, L. Emsley, J. V. Milić, M. Grätzel, *J. Am. Chem. Soc.* **2020**, *142*, 1645.
- [58] G. C. Papavassiliou, G. A. Mousdis, C. P. Raptopoulou, A. Terzis, *Z. Naturforsch., B: J. Chem. Sci.* **1999**, *54*, 1405.
- [59] T. Schmitt, S. Bourelle, N. Tye, G. Soavi, A. D. Bond, S. Feldmann, B. Traore, C. Katan, J. Even, S. E. Dutton, F. Deschler, *J. Am. Chem. Soc.* **2020**, *142*, 5060.
- [60] J. C. de Mello, H. F. Wittmann, R. H. Friend, *Adv. Mater.* **2004**, *9*, 230.
- [61] R. T. Ross, *J. Chem. Phys.* **1967**, *46*, 4590.
- [62] P. Caprioglio, M. Stolterfoht, C. M. Wolff, T. Unold, B. Rech, S. Albrecht, D. Neher, *Adv. Energy Mater.* **2019**, *9*, 1901631.
- [63] W. Tress, M. Yavari, K. Domanski, P. Yadav, B. Niesen, J. P. C. Baena, A. Hagfeldt, M. Graetzel, **2018**, *11*, 151.
- [64] T. Kirchartz, J. A. Márquez, M. Stolterfoht, T. Unold, *Adv. Energy Mater.* **2020**, *10*, 1904134.